Vertical distribution of ice crystals in Arctic mixed-phase clouds derived from airborne spectral radiation measurements

André Ehrlich[1], Eike Bierwirth[1,5], Manfred Wendisch[1], Jean – Francois Gayet[2], Guillaume Mioche[2], Steffen Beirle[3], Thomas Wagner[3], Bernhard Mayer[4]

[1] Institute for Atmospheric Physics, Johannes Gutenberg University, Mainz, Germany
[2] Laboratoire de Météorologie Physique (LaMP), Université Blaise Pascal, Aubière Cedex, France
[3] Max Planck Institute for Chemistry, Mainz, Germany
[4] Institute for Atmospheric Physics, German Aerospace Center, Oberpfaffenhofen, Germany
[5] now at Laboratory for Atmospheric and Space Physics, University of Colorado, Boulder, USA

1. Introduction

Arctic Boundary-Layer Mixed-Phase (ABM) Clouds

- Clouds (especially low-level) most important contributor to Arctic surface radiation budget
- Cloud radiative forcing is highly variable and depends on:
  cloud water content, fractional ice water content, cloud particle size, surface albedo, aerosol

Ice Crystals in ABM Clouds

- Ice crystal properties one essential factor determining the development and persistence of ABM clouds
- Ice nucleation rate and depletion rate control the life time of ABM clouds
- Uncertainty in cloud dynamic modeling due to ice crystal nucleation processes

➔ Information on the vertical distribution of ice crystals is needed
Global coverage ➔ Remote Sensing

2. SMART-Albedometer

(Spectral Modular Airborne Radiation measurements sysTem)

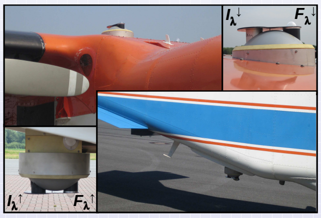

Fig. 1: The SMART-Albedometer mounted on the Polar 2 research aircraft. Close-ups show the optical inlets for irradiance F_λ (transparent semi-spheres) and radiance I_λ (flat opening). The gray cupola holding the inlets is automatically tilted for fast and accurate horizontal stabilization during flight.

Horizontal Stabilization of the Optical Inlets [1]

- Necessity for Arctic (θ_S = 70°) $\Delta\theta$ = 0.2°→ ±2% deviation in $F_\lambda\downarrow$
  $\Delta\theta$ = 1.0°→ ±5%

Active system using servo motors
- Range ± 6°, Accuracy of 0.2°
- Time response 43 ms for angular velocities up to 3°s^{-1}

Radiation Measurements

- 6 grating spectrometers
- 4 optical inlets for radiance I_λ and irradiance F_λ

Spectral Cloud Top Reflectance

$$R(\lambda) = \pi I_\lambda^{\uparrow} / F_\lambda^{\downarrow}$$

	Measured Quantity	Spectral Range	Resolution
Airborne	Downwelling Irradiance $F_\lambda\downarrow$	310-1000 / 1000-2200 nm	2-3 / 9-16 nm
	Downwelling Radiance $I_\lambda\downarrow$	310-1000 nm	2-3 nm
	Upwelling Irradiance $F_\lambda\uparrow$	310-1000 nm	2-3 nm
	Upwelling Radiance $I_\lambda\uparrow$	310-1000 / 1000-2200 nm	2-3 / 9-16 nm

3. ASTAR 2007 (Arctic Study of Tropospheric Aerosol, Clouds and Radiation)

- Campaign organized by Alfred Wegener Institute for Polar and Marine Research (AWI)
- Northern flow of cold air outbreak initiated convection over the warm ocean
  ➔ boundary-layer mixed-phase clouds
- In situ measurements (Polar Nephelometer, FSSP-100, CPI)
- Mixed-phase clouds showed liquid layer at cloud top precipitating ice below

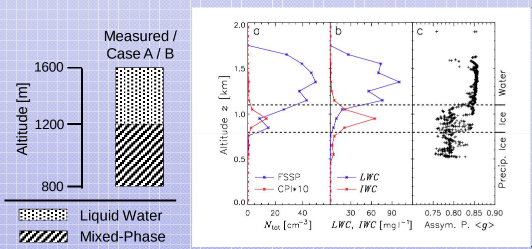

Fig. 3: Cloud representation in the radiative transfer simulations (left panel). In situ measurement (April 7) of ice crystal and liquid water droplet concentrations (a), liquid water content and ice water content (b), and asymmetry parameter (c)

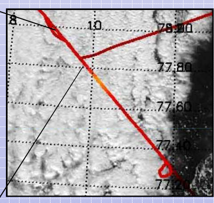

Fig. 2: Extract of the flight track of April 7 along the CALIPSO track overlaid on the MODIS satellite image.

Radiative Transfer Simulations

- Radiative transfer simulations of R, libRadtran, DISORT 2, 1-dimensional, plan parallel
- Scaling of in situ measurements used as model input is necessary to obtain the measured R at λ < 1400 nm
- Cloud optical thickness is underestimated due to cloud inhomogeneities
- Higher ice absorption observed than modeled (1450 - 1600 nm wavelength)
- Variation of ice optical fraction (Case B0-6) does not improve the simulations ($f_i^* = \tau_i / (\tau_i + \tau_w)$)

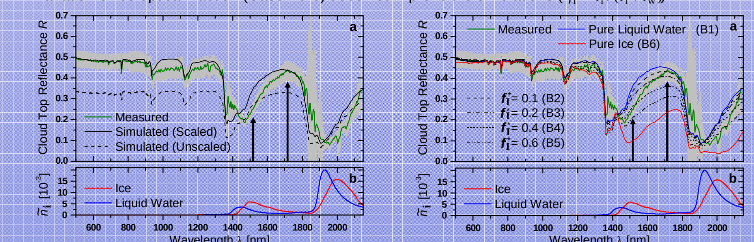

Fig. 4: Measured and simulated cloud top reflectance using measured and scaled (Case A) cloud properties (left panel). Results for Case B0-6 are shown in the right panel. Measurement uncertainties are indicated by the gray area. The imaginary part of the refractive index is given in panel b.

4. Vertical Footprint of Reflectance Measurements

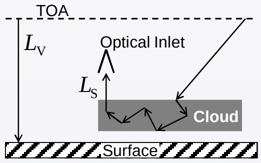

Fig. 5: Definition of air mass factor.

Air Mass Factor

- Characterizes photon path length L_S in the atmosphere and cloud
- Enhanced photon paths imply enhanced scattering and thus enhanced absorption by cloud particles

➔ Air mass factor provides a measure for absorption by cloud particles

$$A = \frac{L_S}{L_V}$$

Fig. 6: Vertical profile of box air mass factor simulated for Case A (upper panel) and the calculated vertical footprint (lower panel) for 1510 nm and 1710 nm wavelength.

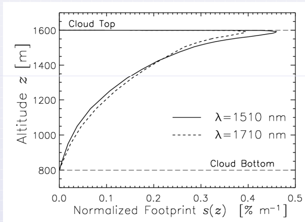

Box Air Mass Factor [2]

- Contribution of distinct cloud layers to the absorption
- assuming vertically homogeneous clouds
  ➔ Vertical footprint s_i

$$A = \frac{1}{N}\sum_{i=1}^{N} a_i \qquad s_i = \frac{a_i}{A}$$

- Simulations with 3-dimensional Monte Carlo model, McArtim
- Cloud input of Case A
- Highest contribution close to cloud top (~10 m below)
- Differences between 1510 nm (high absorption) and 1710 nm (weak absorption)

➔ 1710 nm higher contribution from lower cloud layers
➔ 1510 nm higher contribution from cloud top layers

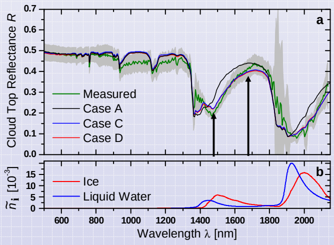

Fig. 8: Measured and simulated cloud top reflectance for Case A, C and D (panel a). Measurement uncertainties are indicated by the gray area. The imaginary part of the refractive index is shown in panel b.

➔ Ice Crystals at Cloud Top

- Strong absorption at 1510 nm indicates ice at cloud top
- Weak absorption at 1710 nm ➔ liquid water below
- Modified cloud (Case C, D) for simulations
- Both cases fit into measurement uncertainties:
  - Strong absorption at 1510 nm
  - Weak absorption at 1710 nm

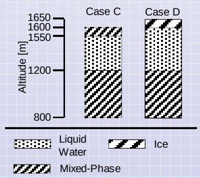

Fig. 7: Cloud representation in the radiative transfer simulations

5. Observation of Backscatter Glory

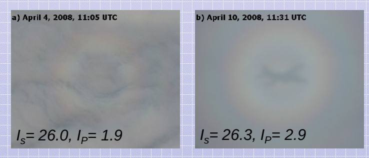

Fig. 9: Photographs of backscatter glories observed during ASTAR 2007 above mixed-phase clouds.

Observation

- Single scattering feature of liquid water droplets
- Backscatter angles larger than 175°
- Indication for liquid water droplets at cloud top
- Simultaneous observation of moderate ice indices

Simulation of Backscatter Glory [3]

- 3-dimensional Monte Carlo code MYSTIC
- Results converted into RGB colors (CIE system)

Results

- Backscatter glories are reproduced by Case A and C, with less pronounced glory for Case C
  ➔ Mixed-phase cloud top layer (Case C) does suit the observations during ASTAR
- Case D dominated by ice crystals phase function (no mixture) located above the liquid water layer
  ➔ This case can be ruled out

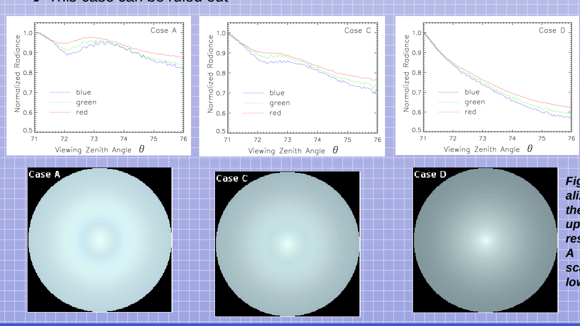

Fig. 10: Simulated normalized spectral radiances in the backscatter region. The upper panels show the results converted into RGB. A visualization of the backscatter glory is given in the lower panels.

6. Outlook

- Further systematic measurements are necessary
- Aircraft measurement campaign SoRPIC (Solar Radiation and Phase Discrimination of Arctic Clouds) in April 2010 / Svalbard
  ➔ Operating SMART-Albedometer on POLAR 5 (AWI)
  ➔ Operating in situ instrumentation (Polar Nephelometer, CPI, FSSP, LaMP)
  ➔ Operating hyperspectral camera system Specim AISA Eagle (AWI)
  ➔ Operating airborne lidar system (AWI)

[1] Wendisch, M., Muller, D., Schell, D., and Heintzenberg, J. (2001). An airborne spectral albedometer with active horizontal stabilization. J. Atmos. Oceanic Technol., 18, 1856–1866.

[2] Wagner, T. et al. (2007). Comparison of box-air-mass-factors and radiances for MAX-DOAS geometries calculated from different UV/visible radiative transfer models. Atmos. Chem. Phys. 7, 1809-1833.

[3] Mayer, B., Schröder, M., Preusker, R., and Schüller, L. (2004). Remote sensing of water cloud droplet size distributions using the backscatter glory: A case study. Atmos. Chem. Phys. 4: 1255-1263.